



LAWRENCE
LIVERMORE
NATIONAL
LABORATORY

Interferometric adaptive optics for high power laser pointing, wave-front control and phasing

K. L. Baker, E. A. Stappaerts, D. C. Homoelle, M. A. Henesian, E. S. Bliss, C. W. Siders, C. P. J. Barty

February 13, 2009

SPIE Photonics West MOEMS-MEMS 2009
San Jose, CA, United States
January 25, 2009 through January 29, 2009

Disclaimer

This document was prepared as an account of work sponsored by an agency of the United States government. Neither the United States government nor Lawrence Livermore National Security, LLC, nor any of their employees makes any warranty, expressed or implied, or assumes any legal liability or responsibility for the accuracy, completeness, or usefulness of any information, apparatus, product, or process disclosed, or represents that its use would not infringe privately owned rights. Reference herein to any specific commercial product, process, or service by trade name, trademark, manufacturer, or otherwise does not necessarily constitute or imply its endorsement, recommendation, or favoring by the United States government or Lawrence Livermore National Security, LLC. The views and opinions of authors expressed herein do not necessarily state or reflect those of the United States government or Lawrence Livermore National Security, LLC, and shall not be used for advertising or product endorsement purposes.

Interferometric adaptive optics for high power laser pointing, wave-front control and phasing

K.L. Baker^{*a}, E.A. Stappaerts^{a,b}, D.C. Homoelle^a, M.A. Henesian^a, E.S. Bliss^a, C.W. Siders^a, C.P.J. Barty^a

^aLawrence Livermore National Laboratory, 7000 East Ave., Livermore, CA, USA 94550-0345

^bStappaerts Consulting, LLC, San Ramon, CA

ABSTRACT

Implementing the capability to perform fast ignition experiments, as well as, radiography experiments on the National Ignition Facility (NIF) places stringent requirements on the control of each of the beam's pointing and overall wave-front quality. One quad of the NIF beams, 4 beam pairs, will be utilized for these experiments and hydrodynamic and particle-in-cell simulations indicate that for the fast ignition experiments, these beams will be required to deliver 50%(4.0 kJ) of their total energy(7.96 kJ) within a 40 μm diameter spot at the end of a fast ignition cone target. This requirement implies a stringent pointing and overall phase conjugation error budget on the adaptive optics system used to correct these beam lines. The overall encircled energy requirement is more readily met by phasing of the beams in pairs but still requires high Strehl ratios, S_r , and rms tip/tilt errors of approximately one μrad . To accomplish this task we have designed an interferometric adaptive optics system capable of beam pointing, high Strehl ratio and beam phasing with a single pixilated MEMS deformable mirror and interferometric wave-front sensor. We present the design of a testbed used to evaluate the performance of this wave-front sensor below along with simulations of its expected performance level.

Keywords: Adaptive Optics, Short-Pulse Lasers, Wave-front sensing, Interferometry

*baker7@llnl.gov; phone 1 925 422-1461; fax 1 925 422-1796

1. INTRODUCTION

Numerous laser systems currently employ, or have employed in the past, adaptive optics (AO) systems to correct their wave-front aberrations. These aberrations can be caused by many mechanisms which include thermal distortions in the amplifiers, temperature fluctuations, stress-induced birefringence, damage spots on and inherent aberrations in the optical components, nonlinear effects, vibrations and misalignment of optics. The laser systems with AO systems include the largest lasers currently being built, the National Ignition Facility¹ and the Laser Megajoule, the beamlet laser, the NOVA petawatt laser,² the beamlet laser,³ the LULI laser system,⁴ the Vulcan petawatt laser,⁵ to name a few. These lasers have exclusively used Shack-Hartmann and shear-interferometer systems which measure the gradient in the wave-front and as such are unable to measure the piston error between multiple beams.

The National Ignition Facility (NIF) will become fully operational this calendar year and will consist of 192 conventional deformable mirrors, one for each of the Nd glass beam lines. A schematic of one of the NIF beam lines is shown below in Fig. 1. The laser light is generated in the master oscillator room and delivered to the 48 separate preamplifier modules (PAM). The PAM has two different amplification stages; the first is a regenerative amplifier resulting in a pulse energy of 15 mJ and the second is a four pass relay imaging rod amplifier which amplifies the pulse energy by an additional factor of up to 10,000. The output of the PAM can vary between 10 mJ to 10 J with a nominal value of 1 J. The MEMS device for the interferometric adaptive optics system will be placed in the beam line at a point where the fluence is below 100 mJ/cm^2 , well below the damage threshold of $\sim 1 \text{ J}/\text{cm}^2$ for gold coated substrates. After amplification in the preamplifier module the laser beam travels to the final two amplifiers which provide 99.99% of the laser's energy. As the beam enters the four-pass cavity amplifier, containing a conventional deformable mirror, the pulse is switched into, and out of the amplifier after the fourth pass through the amplifier, using a plasma-electrode Pockel cell and then transported to the target chamber where it is converted to the third harmonic and focused onto the inside walls of the Hohlraum placed at target chamber center. A Shack-Hartmann wave-front sensor is used to control each of the individual conventional deformable mirrors.¹ The mirrors, however, contain only 39 actuators and hence correct for

relatively low order aberrations. Fig. 2 shows, in the figure on the left, a simulated conjugate phase profile for the Shack-Hartmann controlled deformable mirror in a NIF beam. The measured uncorrected residual phase is shown in the middle image and the simulated far-field is shown in the image on the right. The simulated Strehl ratio resulting from the residual phase is ~ 0.5 . The Shack-Hartmann wave-front sensor measures the wave-front at the exit of the transport spatial filter and hence does not include aberrations in the final optics of the laser chain.

The NIF alignment and wave-front control systems have performance requirements for positioning each of the NIF beams to within a $\leq 50 \mu\text{m}$ RMS spot position at target chamber center.¹ High speed measurements taken on one of the NIF beamlines indicated that over a 12.5 second window the observed RMS displacement of the spot at target chamber center from mean was $< 17 \mu\text{m}$. The measurements were taken at a rate of 1.3 khz and indicated peaks in the vibrations between 20-60 hz.¹ In addition these measurements were taken between the transport spatial filter and the target chamber center.

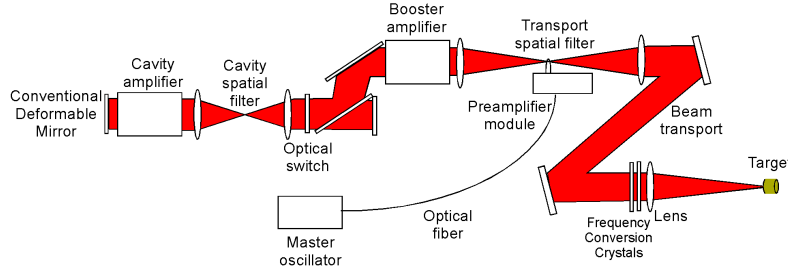


Fig. 1. Schematic of the major components of a National Ignition Facility (NIF) laser beam from injection to final focus.

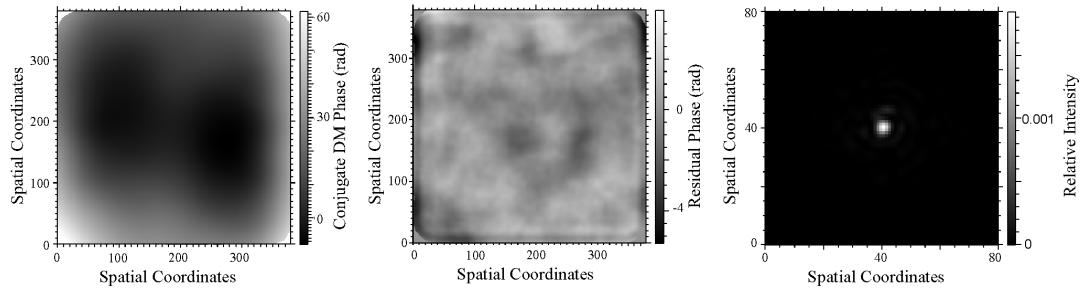


Fig. 2. Conjugate phase profile for the Shack-Hartmann controlled deformable mirror in a NIF beam. The uncorrected residual phase is shown in the middle image and the resultant far-field is shown in the image on the right. The Strehl ratio resulting from the residual phase is ~ 0.5 .

1.1 Short pulse capability on the National Ignition Facility

One quad of the 192 NIF beams, four beam pairs, are designated for x-ray backlighting and fast ignition experiments. The x-ray backlighting capability is designated as the advanced radiography capability, ARC, on the NIF laser and the fast ignition delivery capability has been named the fast ignition drive optics, FIDO. These beam lines will differ from the standard NIF beam line in several ways. A fiber-based short pulse will be added to the master oscillator to seed a quad of main amplifiers. The short pulse is stretched in pulse length before entering the preamplifier modules and then compressed to a 5 ps pulse with a vacuum compressor placed on the target area mezzanine. The short pulse will then be focused near target chamber center with an off-axis parabola to minimize B integral effects. Each of these four beam pairs will deliver a laser pulse to chamber center that is nominally 5 ps in pulse length and 1.99 kJ in energy, giving an overall energy of 7.96 kJ delivered to the target. The x-ray backlighting capability requires better control of the beam wander than achievable with the existing AO system to maximize the number of successful experiments, ensuring that the backlighter is within the field-of-view of the x-ray diagnostics. This necessitates better control of the tip/tilt component of the ARC beam lines. In addition, improving the Strehl ratio of the beams would dramatically improve the signal-to-noise ratio of the x-ray radiography experiments and thereby improve the scientific results obtained with this diagnostic. The fast ignition experiments, however, require that 4 kJ of the total 7.96 kJ of laser energy be deposited within a $40 \mu\text{m}$ diameter circle. The pupil geometry of the four beam pairs is shown below in Fig. 3a along with the far-field pattern, in Fig. 3b, generated by this pupil assuming that each of the beams are in phase with no phase aberrations

are present. Fig. 3b also contains a 40 μm diameter circle showing the spatial dimensions of the focused beams. A schematic of the fusion target is given in Fig. 4. The four beam pairs will pass through the gold cone, ~ 30 degree acceptance angle, attached to the fusion capsule and focus at the end of the cone, a roughly 40 μm diameter spot. Due to the grazing incidence nature of the fast ignition cone, a percentage of the light that first strikes the edges of the cone will undergo grazing incidence reflection from the surface and refraction through the plasma generated by this interaction and continue down the fast ignition cone and strike the end of the cone. In addition a percentage of the electrons formed when the laser hits the sides of the fast ignition cone will likewise will end up in the appropriate volume to assist in hot spot ignition within the assembled fuel.

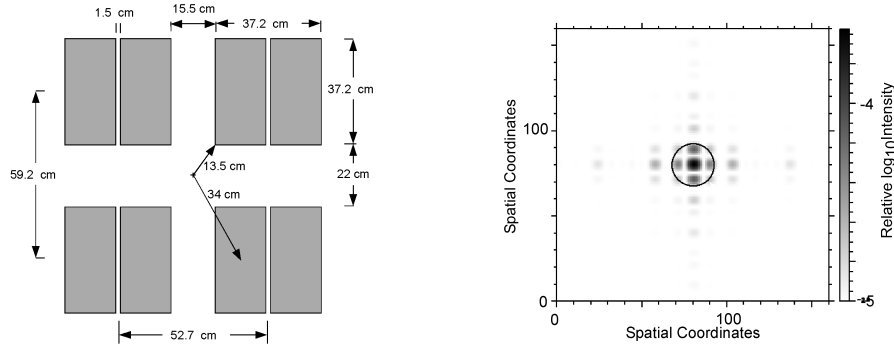


Fig. 3. Pupil layout for the advanced radiography capability on the National Ignition Facility is displayed in Fig.3a. The pupil represents four beam pairs with each of the beam pairs containing 1.99 kJ centered around 1.053 μm in a 5 ps pulse. Fig. 3b shows the far-field pattern generated from this pupil assuming that all of the beams are pistoned correctly and have a perfect Strehl ratio.

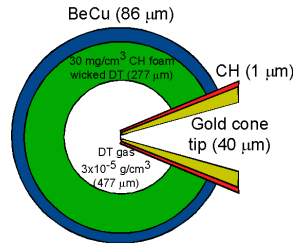


Fig. 4. Fast ignition target geometry. The eight beams must be accurately focused at the end of a gold cone.

The performance of the adaptive optics system in terms of “tip/tilt removed” Strehl ratio, rms tip/tilt error and intrabeam phasing can be studied with simulations introducing random phasing and tip/tilt errors to the 8 beams and looking at the energy encircled within the 40 μm diameter circle in the far-field. If all the beams are phased and pointed together and fully corrected with a Strehl ratio, S_r , of 1, then they would deliver 5.6 kJ in a 40 μm diameter circle, exceeding the requirements by 1.6 kJ. Placing random uniformly distributed piston errors, between 0 and 2π rad, on the 8 beams, however, caused the energy to fall below the requirements given above. Figure 5 represents a study of piston, tip/tilt and higher order turbulence applied to the eight apertures in Fig. 3 above. A thousand iterations were run with the criteria of exceeding a given energy level, plotted in Fig. 5, in 90% of the shots. This approach was used to evaluate the system performance with both random piston errors, random tip/tilt errors and the residual turbulence profile in Fig. 2b applied to the apertures. In the case of tip/tilt errors, normally-distributed pseudo-random numbers with a mean of zero and a standard deviation of one were assigned to both the tip and tilt components of the phase. The system performance as a function of tip and tilt errors were studied again with uniformly distributed piston errors on either the eight beams or with the two beams comprising a beam pair pistoned together. In the case of random phasing errors distributed to all eight beams, labeled as random pistons(dashed lines), even with a system Strehl ratio of 0.95 the encircled energy within 40 μm is only 3.4 kJ. In the case of correct phasing of the two beams within a given beam pair, labeled as random pairs(solid lines), the system Strehl ratio must be greater than 0.72 to exceed the encircled energy requirement of 4 kJ. Again this neglects the laser energy that although first striking the walls of the fast ignition cone, end up hitting the bottom of the cone.

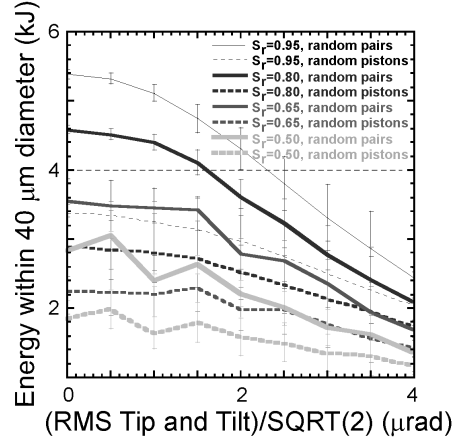


Fig. 5. Ninety percent energy contained within a 40 μm diameter spot as a function of random tip and tilt errors applied to either the four pairs of apertures, solid lines, or the eight individual apertures, dashed lines. Ninety percent energy in this context implies that 90% of the shots exceeded this encircled energy and 10% of the shots fell below this encircled energy. The different colors represent the Strehl ratio obtained by the adaptive optics system; the colors, black, dark gray, light gray thick lightest gray represent Strehl ratios of 0.95, 0.8, 0.65 and 0.5, respectively.

A tip/tilt of 1 μrad at target chamber center corresponds to a total tip/tilt phase across the 37 cm length of the aperture of 0.35 waves and across the 15.6 cm width of the aperture of 0.15 waves. The segmented MEMS is capable of providing a tilt with a Strehl ratio of greater than 50% with two actuators per wave or a range of ± 16 microns. A continuous sheet MEMS with a 3 μm stroke can in principle achieve a high Strehl for ± 6 μm in phase.

1.2 Previous work on interferometric adaptive optics systems

The adaptive optics system detailed below is based on an interferometric adaptive optics system developed under a DARPA proposal called the Coherent Communications, Imaging and Targeting project or CCIT.^{6,7,8} This project developed both the interferometric adaptive optics system at Lawrence Livermore National Laboratory and also the MEMS deformable mirrors at Boston Micromachines Corporation. Several interferometric adaptive optics systems were designed and built under this project with the final system implemented on a 1.3 km open-air path to compensate for atmospheric aberrations in real time. This AO system was based on a quadrature Twyman-Green interferometer that operated at a wavelength of 1.5 μm and achieved correction speeds in excess of 1 khz. This wave-front sensor utilized quadrature interferograms, allowing reconstruction of the wave-front over the range of 0 to 2π radians. The system operated in open-loop, where open-loop in this context means that the correction applied to the spatial-light-modulator in the previous pass through the loop was not sensed by the interferometer. One advantage of open-loop operation is an increased correction bandwidth. The CCIT adaptive optics system achieved correction speeds in excess of 1 khz and Strehl ratios greater than 0.5 with Kolmogorov phase screens. The original prototype MEMS-based spatial light modulator used in this AO system had approximately 60 bad pixels and the outer actuators were not activated giving nearly 18% of the actuators that were not contributing to the correction. Wave optics simulations performed using a bad pixel map of the actuators indicated that the non-activated pixels caused a reduction in the Strehl ratio of approximately 22%.

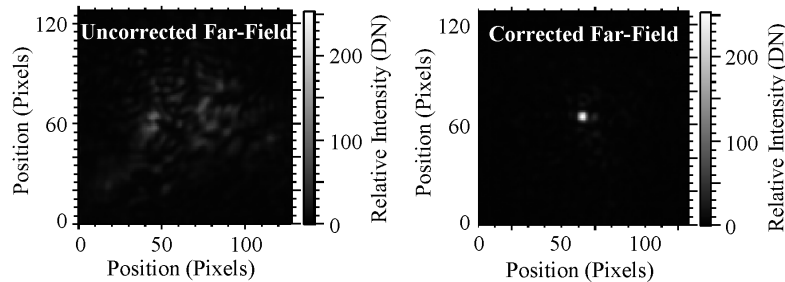


Fig. 6. Point-spread-functions for the uncorrected and corrected probe beams in the CCIT AO system.

2. TESTBED DESIGN

The optical layout of the IR laboratory breadboard system is shown in Figure 7. It consists primarily of an interferometric wave-front sensor, a MEMS-based spatial-light-modulator built by the Boston Micromachines Corporation (BMC), two tip/tilt mirrors, an Nd:YLF laser and computer hardware/software to analyze the wave-front and implement the phase correction. The system can be run in either open or closed-loop operation. The laser source is split into three separate beams using polarizing beamsplitters and has a nearly transform-limited pulse of 2 ns duration and a pulse energy of 35 μJ . The testbed is designed to evaluate the performance in both open and closed-loop for the MEMS device and can also evaluate the performance of both segmented and continuous phase sheet MEMS devices. The segmented devices do not require a wave-front reconstruction, however, the continuous phase sheet MEMS devices will require a wave-front reconstruction to be performed.

Polarization components are utilized in the testbed to form the two interferograms with a $\pi/2$ phase shift between them and also to control the relative signal levels in the arms of the interferometer. The probe beam passes through a square aperture that is relay imaged onto the MEMS-based spatial light modulator in open-loop operation. As it travels to the MEMS device the probe beam is transmitted through aberrating phase plates that were designed to simulate the laser's turbulence with a Kolmogorov turbulence spectrum. The MEMS device is then relay imaged onto the partial reflector, APR, which is relay imaged onto the focal plane array. At the APR a percentage of the probe beam is reflected and travels back upstream to a beam splitter which sends part of the probe into the interferometric wave-front sensor where it is combined with the reference beam. The reference beam passes through a third thin film polarizer near the top of Figure 7 and the resulting p-polarized beam passes through a quarter wave plate (QWP) at 45 degrees to vertical, which converts the linearly polarized light into circularly polarized light. After passing through the QWP, the reference and probe beams, in either the open or closed loop geometries, are combined using a non-polarizing 50/50 beamsplitter. Both beams then pass through a half wave plate that rotates their polarization by $\pi/4$, producing equal amplitude horizontal and vertical components of the probe beam while maintaining the $\pi/2$ phase shift between the horizontal and vertical components of the reference beam. The reference and probe beams then pass through a telescope. A Wollaston prism, at the focus of the first telescope lens, separates the two interferograms in angle. The two interferograms, having orthogonal polarizations, exit the Wollaston prism at an angle of approximately 1.93 degrees with respect to one another and are collimated by the two lens placed directly after the Wollaston prism. The two spatially separated interferograms are then directed to the IR camera, which is in a conjugate plane to the spatial light modulator and to the entrance aperture of the system. Part of the probe beam passes through the APR and is relay imaged to the position of the MEMS device in closed-loop. This plane is then relay imaged onto two subsequent tip/tilt mirrors, one used to simulate vibrations and the other to correct the simulated vibrations. The last tip/tilt mirror is then relay imaged to a plane where additional phase plates add turbulence onto the beam. This plane is relay imaged onto the focusing optic, a 1 m f.l. lens, which then focuses the probe beam onto the target. Tracking cameras are used to measure the Strehl ratio and the tip/tilt correction of the system and an additional tracking camera is placed upstream of the tip/tilt mirrors to evaluate offloading of the tip/tilt correction with a CCD camera by tracking the spot motion.

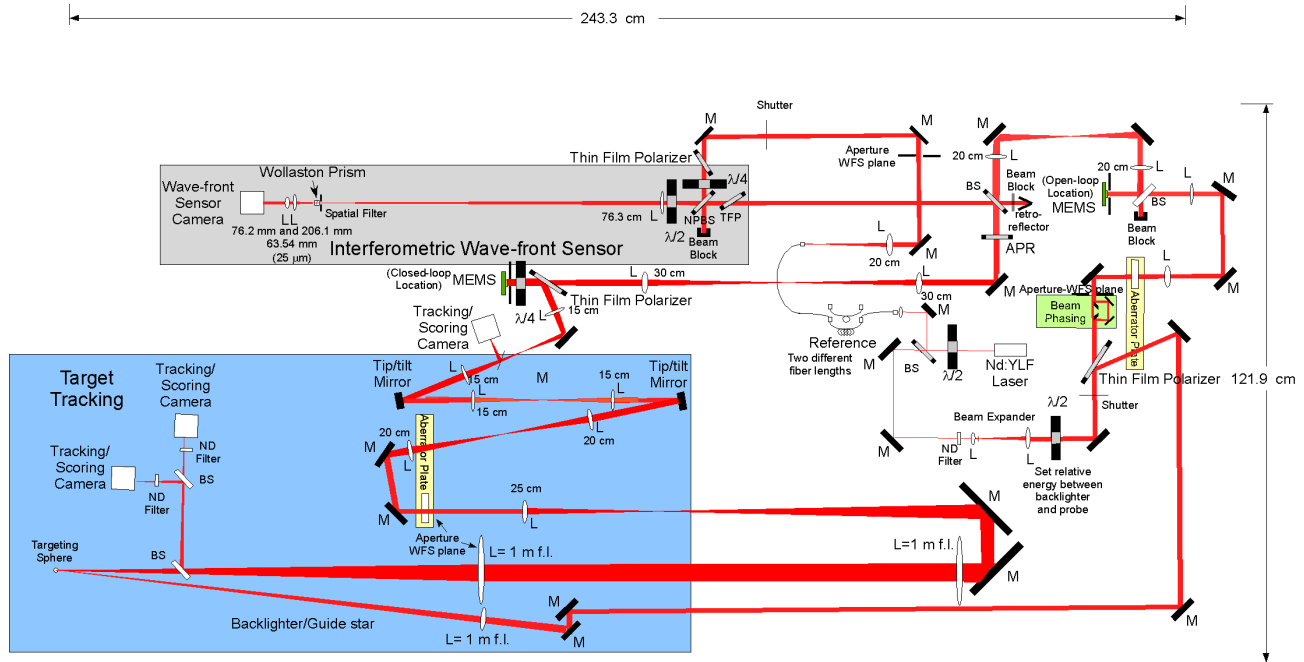


Fig. 7. Laboratory breadboard setup used to test the performance of the phase conjugate engine in a controlled laboratory environment. The abbreviations stand for the following: BS, beam splitters; M, mirrors; L, lenses; S, shutters; A, apertures; TFP, thin film polarizers; $\lambda/2$ and $\lambda/4$, half and quarter wave-plates, respectively.

The two interferograms provide the sine and cosine channels, however, additional information is required to unwrap the phase. These two interferograms contain three unknowns, the reference beam electric field, the probe beam electric field and the phase. To provide additional information, the reference aperture is oversized relative to the probe beam. By measuring the spatial profile of the reference beam before the shot and using the oversized region on the detector to set the appropriate amplitude, the detector effectively provides a measurement of the reference beam intensity on each shot as well. By setting the probe beam intensity much lower than the reference beam and neglecting this component in the interferograms, the phase can be uniquely determined.

The testbed will allow testing of many of the algorithms and procedures that would be implemented on the NIF laser. The testbed will enable simulation of the interferometric adaptive optics system in either closed or open-loop geometry and allow the study of correcting multiple aperture piston and tip/tilt aberrations in addition to higher order aberrations. Algorithms for offloading tip/tilt from the wave-front sensor measurement to a tip/tilt mirror will be tested. Testing the open-loop addition of upstream and downstream corrections and alignment procedures will also be examined. The scenario of running the interferometric adaptive optics system for high-order correction and a separate quad-cell for tip/tilt correction after the interferometric adaptive optics system has been set will also be tested.

2.1 Alternative interferometric wave-front sensing designs

The baseline wave-front sensor described above utilizes a $\lambda/4$ waveplate to create a circularly polarized reference beam and then separates the orthogonally polarized components of both the reference and probe beams with a Wollaston prism onto the wave-front sensor camera. This design is also shown below in Fig. 8a. An alternative design produces four phase shifts on the wave-front sensor camera. The alternative design uses more space on the wave-front camera and therefore is slower to readout from the camera. The alternative design is similar to one reported in ⁹.

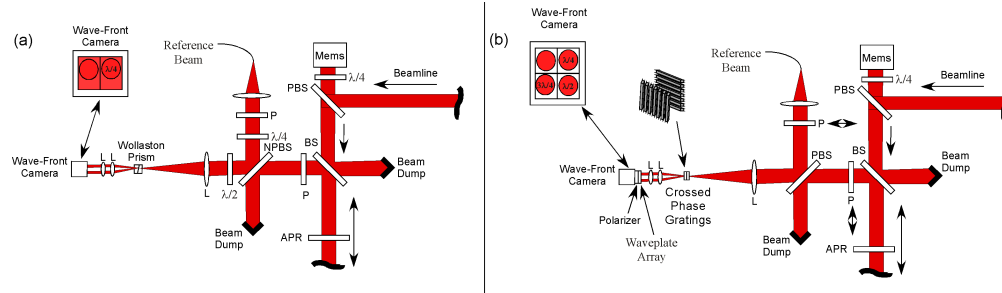


Fig. 8. Comparison of two approaches to the interferometric wave-front sensor in an open-loop geometry. Fig. 8a uses a Wollaston prism to produce two channels on the wave-front camera with the reference beam having a $\pi/2$ phase shift between the two channels. Fig 8b uses two crossed phase gratings to produce four copies of orthogonally polarized reference and probe beams. A waveplate array subsequently produces a phase shift of 0, $\pi/2$, π and $3\pi/2$ between the reference and probe beams in the four copies and a polarizer allows the two beams to interfere on the wave-front camera. The abbreviations stand for the following: BS, beam splitters; NPBS, non-polarizing beam splitters; P, polarizers; L, lenses; $\lambda/2$ and $\lambda/4$, half and quarter wave-plates, respectively.

2.2 Planned correction of the ARC/FIDO beam line (How the interferometric system will work)

The correction of the ARC/FIDO beam lines will happen in several stages. The MEMS device and interferometric wave-front sensor will be located at relay plane 10 in the ARC beam line at the preamplifier module. Initially the aberrations upstream of the wave-front sensor will be measured by placing a partial reflector in the system just downstream of the wave-front sensor. An interferogram of the wave-front aberrations in the laser to this optic will be recorded and added to the wave-front sensor measurement of the rest of the laser in open loop to enable the full correction of the ARC/FIDO beam. The alignment procedure for the partial reflector is shown below in Fig. 9. The delay of the reference beam will be set to initially form an interferogram with the incident laser reflecting from the partial reflector and later with the return signal from target chamber center. Commercial corner cubes have retroreflected parallelism accuracies of less than half an arcsecond or $<2.4 \mu\text{rad}$ and can be aligned to less than a μrad with multiple measurements.

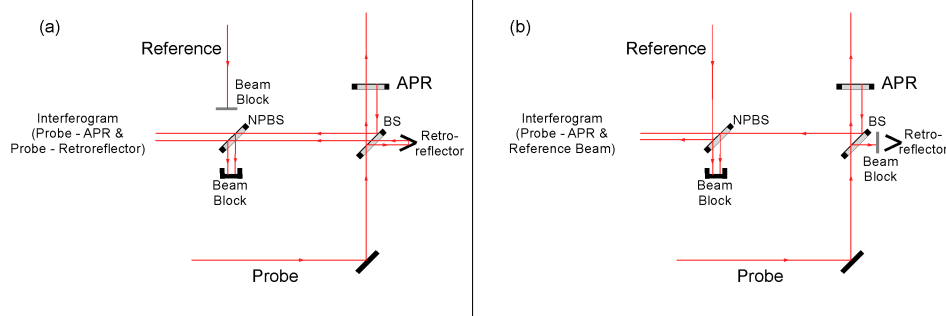


Fig. 9. Alignment procedure. The first step is to align the APR perpendicular to the laser by interfering the laser reflection from the APR with a reflection from a corner cube and removing the tip/tilt as shown in Fig. 9a. The second step is to record the interferogram from the probe laser and the reference beam as shown in Fig. 9b.

The second stage of correction involves placing a targeting sphere or fiber optic backlighter at the entrance to the targeting cone or ARC backlighting target and reflecting a target illumination laser off of the sphere or sending the laser through a single mode fiber as shown in Fig. 10 below. The signal will then travel upstream through the laser chains where it will form an interferogram with the reference beam. There are several scenarios of operation for this second stage. One is that the interferometric adaptive optics system is run at a high rate, $> 5 \text{ kHz}$, such that the aberrations induced by the flashlamp heating of the rod and disk amplifiers are accounted for. In this scenario the wave-front correction measured in this stage is simply added to that of the first stage in open-loop as well as the contribution to the third stage detailed below. This would be the ideal mode of operation as the interferometer would measure the piston, tip/tilt and higher order phase aberrations immediately before the shot. This would, however, likely require a redesign of the electronics driving the plasma-electrode pockel cell (PEPC) as discussed below in the photometry section. The

second scenario is that the interferometric adaptive optics system is not run close enough to shot time to include aberrations due to the flashlamp pumping of the amplifiers which would require operation at greater than 3 kHz (~ 300 μ sec). This correction will be accounted for by taking the difference between an interferometric wave-front measurement taken before the flashlamps are fired and one taken at the normal shot time, both with the NIF deformable mirror actuated. The difference of these two measurements will be added to the upstream interferometric measurement in the first stage and to the interferometric measurement taken at each shot before the flashlamps are fired. For this latter scenario a phase plate would be required in the wave-front sensor to effectively null out the contribution of the existing deformable mirror, Fig. 2a, for the measurement taken before the flashlamps are fired as detailed below in the simulations section. The conventional deformable mirror is set approximately 1 hour before the laser shot. For interferometric measurements taken seconds before the flashlamps are fired, additional diagnostics such as a quad-cell or a small CCD with correlation tracking could be used in the transport spatial filter, downstream of the PEPC, to provide high speed tracking of the tip/tilt motion from the sensor to target chamber center which can then be added to the MEMS device in open-loop.

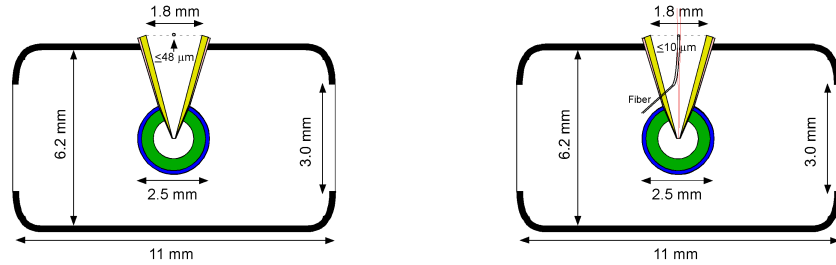


Fig. 10. Hohlräum geometry for fast ignition targets. Target alignment ball placed at the top of the fast ignition access cone in the figure on the left and a fiber illuminator is inserted into the cone on the figure on the right. A sub-diffraction limited targeting sphere, circle or fiber is placed in the center of the top of the fast ignition access cone. The target illumination laser then scatters from the targeting sphere or passes through the fiber and sends the probe beam back through the laser chains to the interferometric wave-front sensors where they interfere with the local reference laser.

The third and final stage of correction involves accounting for the offset and distance between the targeting sphere and the desired focal spot at the end of the fast ignition cone. This involves placing a slight tip/tilt and focus term on each of the beams to steer the beams off of the targeting sphere and correct the $\sim 5 \times 10^{-4}$ change in the focal length. The change in tip/tilt between the individual beams focusing on the targeting sphere and the end of the fast ignition cone is slight, $\alpha(\Delta x/f.l.)$, where α is the angle of the guide star beam from the optical axis of the ARC pupil, $f.l.$ is the focal length of the parabola and Δx is the distance between the targeting sphere and the end of the fast ignition cone. For each of the beam pairs forming the ARC pupil this corresponds to an applied tilt of 18.8μ rad or a peak-to-valley phase tip/tilt of 6.9μ m. The difference in the focal length imposed on the MEMS devices to make the required changes to the focus of the parabola is a peak-to-valley defocus of 0.66μ m. The application of the tip/tilt phase of 6.9μ m will result in a slight reduction in the Strehl ratio as shown in Fig. 11 below. This figure shows the range of motion that a piston-only MEMS mirror possesses with 32 actuators, given a pupil of 37 cm and a focal length of ~ 900 cm. As the number of actuators per wave is decreased, there is a reduction in the achievable Strehl ratio. As that number reaches two actuators per wave the MEMS device becomes a phase grating with a 180 degree phase shift between adjacent pixels and an efficiency in the +1 order is $\sim 43\%$. The Strehl ratio can be approximated as $S_r \sim \text{EXP}\{-(\pi^2/3)(\text{Amp}/32)^2\}$, where 32 represents the number of MEMS rows and Amp represents the number of waves of tilt across the MEMS device.¹⁰ The performance can be increased dramatically by going to a MEMS device which is capable of piston and tip/tilt of the individual actuators in which case the pointing would be increased to the angular capacity of the spatial filters within the laser itself, $\sim 200 \mu$ rad, without a loss in the Strehl ratio.

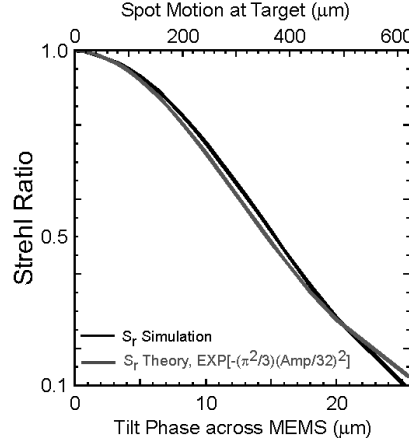


Fig. 11. Reduction in Strehl ratio as a function of tilt applied to the MEMS device. In the case of a 37 cm aperture with a ~900 cm f.l. lens, the resultant spot motion at target is shown along the upper horizontal axis.

The NIF laser beam will have a fluence of $\sim 100 \text{ mJ/cm}^2$ on the MEMS mirror. Given this fluence, the amount of light that would be coupled into the wave-front sensor with a half of a percent pickoff would be 500 μJ with 125 μJ impinging upon a 32×32 region of the wave-front sensor. That corresponds to 122 nJ per pixel or $(122 \times 10^{-9} \text{ J}) / (1.053 \times 10^{-6} \text{ m}) / ((6.626 \times 10^{-34} \text{ J/sec})(3 \times 10^8 \text{ m/sec})) = 6.5$ billion photons/pixel, far greater than the full well capacity of 750 thousand electrons. As such on the ARC system the APR will be removed after measurement of the first stage aberrations.

2.3 Photometry requirements for the target illumination laser

The target illumination laser has the task of illuminating a sphere or circle near target chamber center or passing through a single mode fiber to create a laser guide star. The targeting sphere itself should be smaller than a diffraction limited spot to reduce speckle, which for a phased beam pair would be $2\lambda f/\# = 51 \mu\text{m}$ where λ is the laser wavelength and $f/\#$ is equal to the focal length, 900 cm, divided by the aperture size, 37 cm, or $f/24$. The angular extent of the collection optics assuming a circular beam of $f/24$, is $\theta = 1/(2f/\#)$ or $1/48$. The solid angle of the optics is $\pi\theta^2$ and the solid angle for a square beam at $f/24$ would be $\sim 4\theta^2$ or $1.7 \times 10^{-3} \text{ sr}$. The percentage of photons collected from the sphere would then be 2.8×10^{-4} . The minimum number of photons required by the wave-front sensor is ~ 10 photons per pixel or $\sim 20\text{k}$ photons on the detector as shown in Fig. 8 above. The targeting sphere is also less than the diameter of the targeting laser by a significant amount, $50 \mu\text{m}/500 \mu\text{m}$, or ~ 0.01 . In addition there are roughly 100 optical surfaces in the beamline with a nominal transmittance of 0.98 or a total transmittance of ~ 0.3 and a beamsplitter that diverts 0.01 of the energy to the interferometric wave-front sensor. That implies a minimum number of photons of $\sim 5 \times 10^{12}$ photons or greater than nhc/λ , $(5 \times 10^{12} \text{ ph})(6.626 \times 10^{-34} \text{ J/sec})(3 \times 10^8 \text{ m/sec}) / (1.053 \times 10^{-6} \text{ m})$ or 1 μJ . A Shack-Hartmann wave-front sensor would require close to 1 mJ to give the same level of performance given the detector noise assumed as discussed below in the simulations section.

The repetition of the targeting laser is dependent on the scenario over which the AO system is run. The flash lamps are fired approximately 300 μsec before the laser is fired and hence the adaptive optics system would have to operate at higher than 3 kHz, in open loop, to measure the effects of the flash lamps on each shot. In addition to the flash lamps, the NIF beam includes a plasma-electrode Pockel cell (PEPC) to protect the laser from back reflections and reduce spontaneous amplified emission. The plasma electrode on the PEPC is activated every 5 seconds for approximately 3 minutes before the shot.¹¹ This involves formation of the plasma electrode $\sim 15 \mu\text{sec}$ before the “nominal” laser shot and a 400 ns, 17kV pulse that activates the PEPC once the laser is within the main amplifier cavity. The existing PEPC electronics would have to undergo a significant redesign to accommodate a plasma formation and high voltage pulse a 100-200 microseconds before the laser pulse. If the interferometric AO system is run for this scenario it would have to operate at an equivalent rate of 5-10 kHz but the targeting laser would only be required to fire a single pulse for the wave-front measurement. A more minor modification to the PEPC electronics, however, would likely allow the PEPC to be fired at a higher rate than the current 0.2 hz. In addition, phase plates could be inserted into the cavity spatial filter to mimic the firing of the PEPC as originally designed in the beamlet laser to enable AO correction with a Shack-Hartmann wave-front sensor 1 second before the shot.¹ In the case that the inteferometric AO system applies its correction several seconds before the laser shot, a separate quad cell detector could be added near the transport spatial filter to measure the

vibration-induced tip/tilt phase between the interferometric measurement and the laser shot. This tip/tilt phase can then be added to the MEMS device right before the shot or used to control a separate tip/tilt mirror. In this case the targeting laser should have a minimum repetition rate of 100 hz if it is being used to send the measurement to the open loop MEMS or ~ 600 hz to control a closed-loop tip/tilt mirror, assuming a maximum noise frequency component of 60 hz.

By making the target a roughened circular target, such that the light is only scattered within the area subtended by the eight beams, at chamber center the percentage of collected photons could be increased by nearly two orders of magnitude to ease the requirements on the target illuminator laser's energy. A single mode fiber acting like a "guide" star would likewise incur a significant photon number advantage over the targeting sphere. The numerical aperture of the collection beam pair is $\sim 1/48$ and the numerical aperture of the "guide star fiber is $1/8$ indicating that each of the four beam pairs would receive $\sim 1/36$ of the photons from the fiber giving it a nearly two orders of magnitude improvement in the required number of photons.

2.4 MEMS testing

The MEMS deformable mirror was tested separately in a carrier frequency interferometer to characterize the pixel response and to test the mirror in closed-loop. The carrier frequency interferometer was implemented in a Twyman-Green geometry as shown in Fig. 12 below. In this interferometer, a polarizing beam splitter separates the reference beam and the probe beam which then reflect off the reference mirror and the MEMS device, respectively. The two orthogonally polarized beams are then recombined on the polarizing beam splitter and a polarizer is then used to interfere the two beams with the MEMS device relay imaged onto the wave-front camera. The carrier frequency technique is a well established interferometric technique capable of determining large phase profiles from a single interferogram and is relatively immune to vibrations.^{12,13} In this technique a tilt is placed on the reference leg of the Twyman-Green interferometer such that a large number of fringes, ~ 100 , are apparent in the interference pattern on the CCD camera. Fourier transforming the interference pattern produces a Fourier spectrum, which has a DC component and an up and down shifted satellite structure due to the large carrier frequency introduced by the applied tilt on the reference leg. By filtering all but the up-shifted satellite structure and shifting this structure back to the origin, the phase is determined. The wrapped phase calculated in this manner is equal to the inverse tangent of the imaginary part divided by the real part of the inverse Fourier transform. The wrapped phase was then unwrapped using a path following algorithm^{14,15,13}

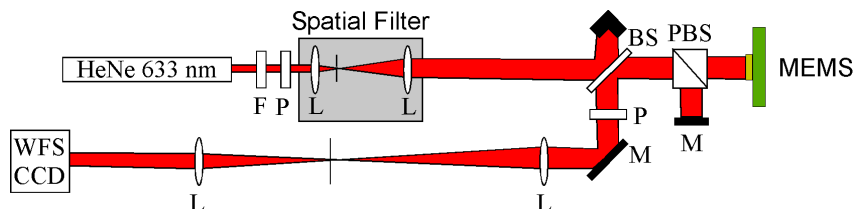


Fig. 12. Twyman-Green interferometer used to characterize the MEMS deformable mirror. The abbreviations stand for the following: BS, beam splitters; M, mirrors; L, lenses; F, filters; PBS, polarized beam splitter; P, polarizers, respectively.

The MEMS device was characterized by energizing half of the MEMS device at multiple voltages, reconstructing the phase profile and then subtracting from the phase of the deenergized MEMS device. By switching between the two halves, the entire MEMS device was characterized at multiple voltage levels. The unpowered MEMS device procured for this testbed is relatively flat over the inner 26 by 26 pixels, however the outer 3 rows and columns have a significant phase curvature due to the polishing procedure in the manufacturing process as seen below in the reflected phase measurement in Fig. 13a. By energizing the MEMS device at multiple voltages and subtracting off the profile shown in Fig 13a, the energized phase profile for each of the actuators as a function of voltage was determined. A polynomial fit of the measured phase vs. voltage was then generated and used to remove the phase profile of the energized MEMS device. The resultant phase is shown below in Fig. 13b. In this case the corrected phase profile had a Strehl ratio of $S_r = 0.88$ at $1.053 \mu\text{m}$.

BMC has several techniques for manufacturing MEMS devices with reduced phase gradients near the edges. One technique is to use a different polishing technique than the one used for this particular MEMS device. Another technique is to produce larger arrays with a sufficient number of sacrificial row and columns such that the inner 32 by 32 pixels of the MEMS device are relatively flat. The current device has 4 sacrificial rows and 4 sacrificial columns. There is also a

technique for epitaxially growing a thick layer of silicon on the mirrors that can then be polished back to produce a significantly flatter profile and can potentially support the stress of a multilayer coating. For the laser application at hand, the latter is the preferred method. With the existing MEMS device either using a smaller portion of the device, 28x28, or using a phase plate would allow for a higher Strehl ratio to be achieved.

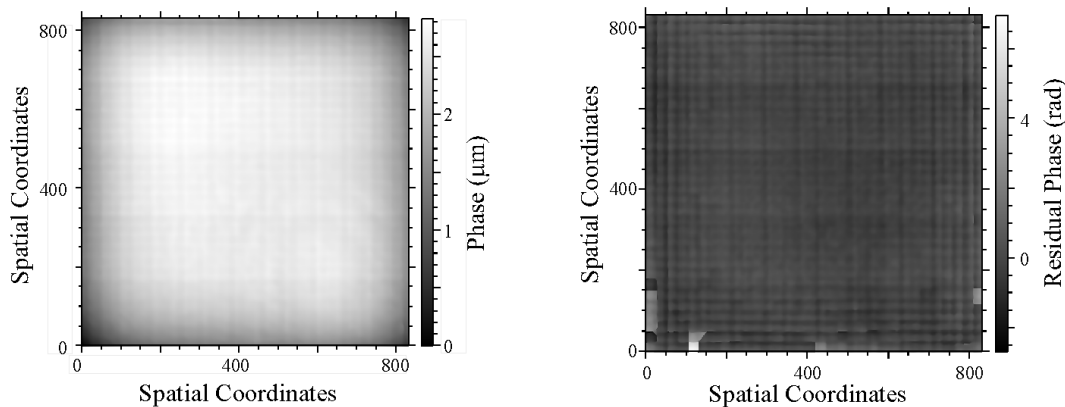


Fig. 13. Reflected phase measurement from the MEMS device with zero volts applied, Fig. 13a, and with the flat field voltages applied after individual pixel characterization, Fig. 13b. The characterization and correction was performed at a wavelength of 632.8 nm.

3. SIMULATIONS

The interferometric adaptive optics system was simulated to better understand both its advantages over conventional adaptive optics systems and its expected performance levels given the expected phase profiles it will encounter. The phase and amplitude profiles used in the simulations were based on actual measurements taken on the NIF laser, as well as PROP simulations of the expected turbulence in the ARC beamline. Fig. 14 shows the measured amplitude and phase for a NIF beamline along with the calculated structure function. A Von Karman spectrum was fit to the structure function as shown in Fig. 15c. The Strehl ratio from the NIF phase is approximately 0.5, however, simulations of the ARC beamline have indicated that the Strehl ratio will be much lower than this value, $S_r \sim 0.09$. For the simulations below, the structure function was increased to match this Strehl ratio. All of the simulations below were performed with a camera gain of 183 ph/adu, a read noise of 300 e- rms and photon noise on the detector.

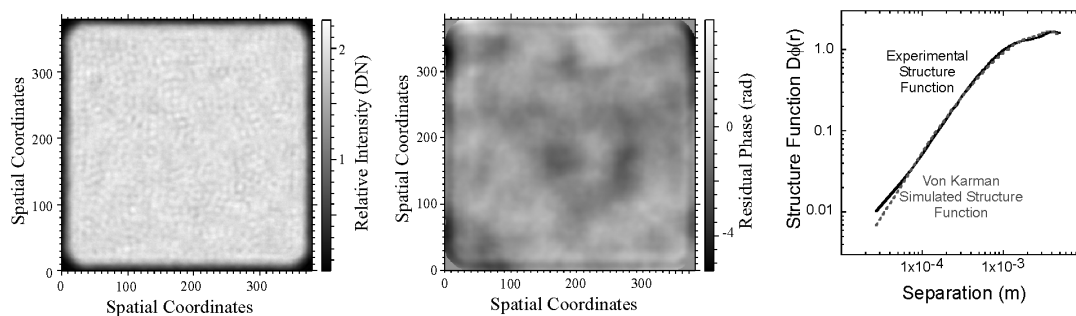


Fig. 14. Measurements of the beam intensity and residual phase for a NIF beam line along with the calculated structure function. Prop simulations of the ARC beamline predict a lower Strehl ratio of $S_r \sim 0.09$. The “Fried” parameter of the structure function in Fig. 14c was increased to produce a Strehl ratio of $S_r \sim 0.09$ for the simulation detailed below.

When the interferometric adaptive optics system measures the laser beam path before the flash lamps have fired, it will measure the NIF DM phase profile before the thermal aberrations have been introduced into the disk amplifiers in addition to the higher order phase aberration in the beam. This is problematic for the interferometric wave-front sensor due to the large phase gradients. Reconstruction of the NIF DM phase profile with the expected residual phase profile for

the ARC beamline is shown below in Fig. 15. The top three figures represent the calculated wrapped phase assuming from left to right, 32, 64 and 128 wave-front sensor pixels across the MEMS device. After the top phases were unwrapped and then binned for the 32 by 32 MEMS, the NIF DM phase was subtracted and the result applied to the MEMS device. The figures on the bottom represent the residual phase difference between what would be applied to the DM and the phase profile of the ARC beamline. The results show that the wave-front sensor would require 128 rows and columns to properly reconstruct the phase of the NIF DM shape before the flashlamps are fired. To eliminate the need for additional wave-front sensor pixels across the MEMS device, a phase plate can be inserted in the probe beam arm of the wave-front sensor to take out the NIF DM phase when the measurement is taken before the flashlamps have fired.

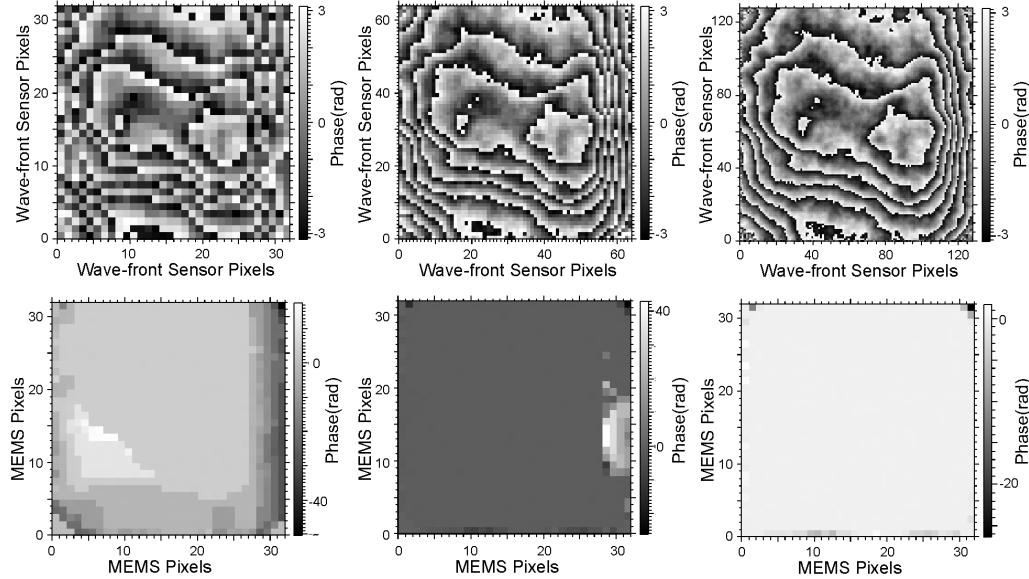


Fig. 15. Reconstruction of the NIF DM phase profile with the expected residual phase profile for the ARC beamline. The top three figures represent the calculated wrapped phase assuming from left to right, 32, 64 and 128 wave-front sensor pixels across the MEMS device. After the top phases were unwrapped and then binned for the 32 by 32 MEMS, the NIF DM phase was subtracted and the result applied to the MEMS device. The figures on the bottom represent the residual phase difference between what would be applied to the DM and the phase profile of the ARC beamline. The results show that the wave-front sensor would require 4 pixels across each actuator to properly reconstruct the phase of the NIF DM shape before the flashlamps are fired.

The Strehl ratio resulting from the measured phase shown in Fig. 15 above was calculated. This involved unwrapping the measured wrapped phase using a path following technique.^{14,15,13} This method locates all of the residues in the wrapped phase by summing wrapped phase differences of four adjacent pixels. If the sum is $\pm 2\pi$, then the pixel is identified as a residue. Branch cuts are generated between the oppositely charged residues. The last step involves a path integration around the branch cuts to determine the unwrapped phase. To test how well the wave-front sensor was able to reproduce the wave-front, the reconstructed phase was subtracted from the NIF DM phase, the MEMS profile and the Von Karman turbulence representing the ARC beamline. The Strehl ratio, calculated by Fourier transforming the field representing the amplitude and residual phase and forming the intensity, from the residual phase is show below in Fig. 16. Even though there is significant residual phase over a fraction of the MEMS device as seen in Fig 15 d and e, the resultant Strehl ratio is relatively high. Only when 128 rows are used on the wave-front sensor is the residual phase over the entire MEMS device kept at relatively low levels. The regions where the phase is not well corrected are due to the steep gradient in the phase in those regions. There are insufficient pixels across a wrapped wavelength to resolve the wave-front and as such those regions are incorrectly unwrapped.

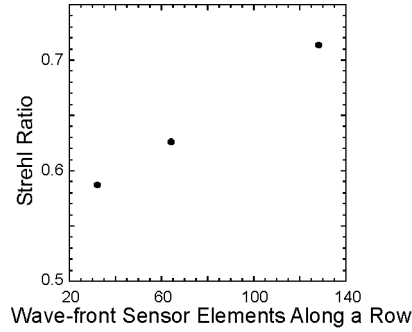


Fig. 16. Strehl ratio as a function of wave-front sensor rows or columns. The reconstructed phase includes the NIF DM phase shown in Fig. 2a as well as a more turbulent Von Karman phase shown in Fig. 14c and the MEMS phase profile shown in Fig. 13a.

The effects of noise, neglect of the probe beam intensity, improper background subtraction and fringing from the detector are shown below in Fig. 17. The figure on the left shows the achievable Strehl ratio as a function of probe photons per pixel. The reduction in Strehl ratio as the number of probe photons per pixel approaches one is due to the decrease in the signal-to-noise ratio with the simulations performed with a camera gain of 183 ph/adu, a full well capacity of 750k e⁻, a reference beam level of 375k e⁻ and a read noise of 300 e⁻ rms. The reduction in the Strehl ratio at higher probe beam levels, above 10k ph/pix, is due to the neglect of the probe beam intensity when determining the phase. The figure in the middle shows the degradation in Strehl ratio which occurs when the reference beam is incorrectly subtracted from the interferograms as would happen for a small error in the measurement of the oversized portion of the reference beam energy. The figure on the right illustrates the effects of fringing fields on the Strehl ratio. Fringing from the detector can occur due to an abrupt change to the index of refraction as from a window on the camera or due to the structure of the focal plane itself. In the simulation, in addition to the reference and probe electric fields two more fields were added before forming the interferograms. In these two additional fields a tilted phase was added to both the reference and probe fields and the amplitude was multiplied by factor of the fringing field multiplier parameter along the horizontal axis in Fig. 17c.

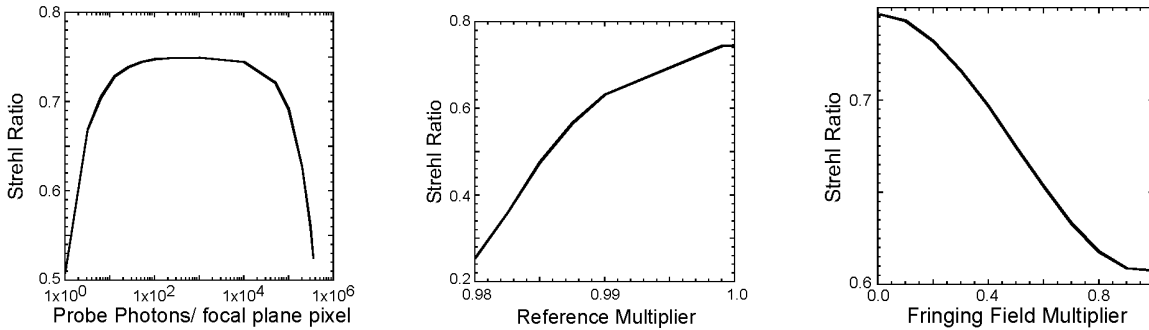


Fig. 17. Performance of the interferometric adaptive optics system on the ARC phase profile. The figure on the left shows the achievable Strehl ratio as a function of probe photons per pixel. The figure in the middle shows the degradation in Strehl ratio that occurs when the reference beam is incorrectly subtracted from the interferograms and the figure on the right illustrates the effects of fringing fields on the Strehl ratio.

The interferometric adaptive optics system was simulated with an ARC beam pair as shown below in Fig 18. Again the higher order residual phases were represented by a Von Karman spectrum with independent phases and tip/tilts applied to the two apertures. The initial phase is given in Fig. 18 a with the resultant far-field shown in Fig. 18b. A representative 40 μ m circle is also drawn in Fig. 18b for scale. When the wave-front is measured and the correction applied to the MEMS device, the corrected far-field is given in Fig. 18c. Fig. 18 a-c were all simulated with a nominal 20 μ rad RMS tip/tilt applied to the two apertures. The three figures on the bottom of Fig. 18 show the corrected Strehl ratios and encircled energy within a 40 μ m diameter along the left vertical axis and the applied tip/tilt to the left and right-hand apertures along the left vertical axis. For small tilts, the corrected Strehl ratio is approximately 74% and the encircled energy percentage is \sim 50%. There is a degradation with both the Strehl ratio and encircled energy as the tilt

level is increased in close accord to the graph in Fig. 11 showing the response of the interferometric system to applied tip/tilt.

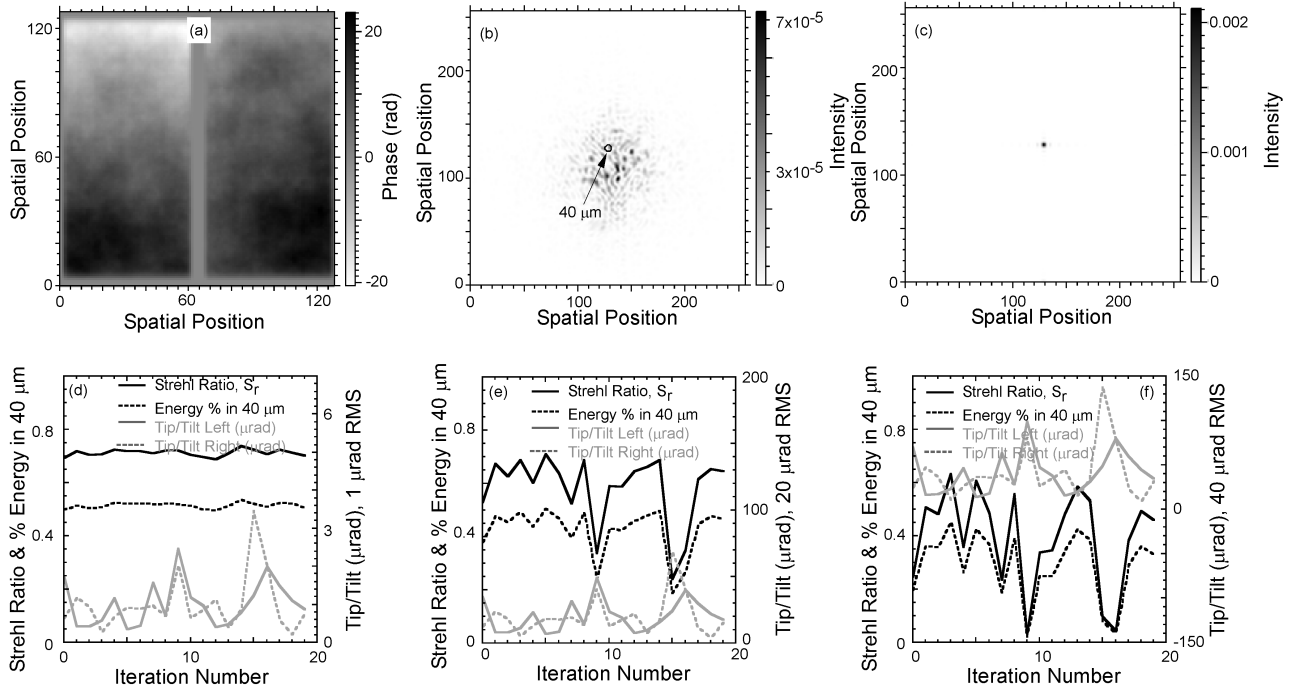


Fig. 18. Simulation of the expected performance of the interferometric adaptive optics system on an ARC beam pair. Fig. 18a displays the initial phase comprised of a tip/tilt error with an RMS value of $20 \mu\text{rad}$, the MEMS residual phase and the Von Karman turbulence profile. Fig. 18b show the resultant far-field distribution given the phase profile in Fig. 18a and the corrected far-field spot is shown in Fig. 18c. The performance of the AO system on an ARC beam pair for random screen generations and different RMS tip/tilt errors are displayed in Fig. 18 d-f with Fig. 18d-f having RMS tip/tilt errors of $1 \mu\text{rad}$, $20 \mu\text{rad}$ and $40 \mu\text{rad}$, respectively. In Fig. 18 d-f the solid black line represents the Strehl ratio of the beam pair, the dashed black line represent the energy encircled within a $40 \mu\text{m}$ diameter circle, the solid gray line represents the tip/tilt coefficient for the left hand pupil and the dashed gray line represent the tip/tilt coefficient for the right hand pupil in μrad .

3.1 Non-interferometric wave-front sensors

Although the interferometric wave-front sensor chosen can achieve the phasing, tip/tilt control and higher order aberration correction with a single wave-front sensor and MEMS deformable mirror, more conventional adaptive optics systems could be used to accomplish these tasks as well. In the latter case, however, multiple wave-front sensors would need to be implemented. In particular, a conventional Shack-Hartmann wave-front sensor could be employed to perform the tip/tilt correction and the higher-order aberration correction. An example calculation of a closed-loop Shack-Hartmann wave-front sensor is shown below in Fig. 19. The phase profile used was the ARC Von Karman turbulence profile and included the initial surface error of the MEMS device itself. By comparing the system performance of the Shack-Hartmann wave-front sensor in Fig. 19 with that of the interferometric wave-front sensor, Fig. 17a, you find that the Shack-Hartmann wave-front sensor requires approximately three orders of magnitude more signal photons than the interferometric wave-fronts sensor, though the Hartmann sensor can reach a slightly higher Strehl ratio due to the use of a continuous sheet deformable mirror.

These wave-front sensors measure the gradient of the wave-front and therefore can not measure the piston error directly. In order to achieve the phasing, however, a separate lenslet array can be employed to measure the piston error between the separate laser beams. This can be done by placing the lenslet across the two separate apertures, effectively interfering the two apertures in the far-field, and measuring the diffraction pattern produced. By comparing the measured diffraction pattern to simulations or adding a grism and measuring the slope of the interferogram, the piston error can be determined. The Keck telescope uses the former approach to piston the hexagonal segments in its primary mirror, albeit pistoning the

segments and taking multiple measurements.¹⁶ This approach allows them to piston the segments to 30 nm rms with an overall capture range of 30 microns. The capture range is equal to $\lambda^2/\Delta\lambda$ and is a function of the laser wavelength, λ , and bandwidth, $\Delta\lambda$. As demonstrated in the simulations above, however, the interferometric wave-front sensor is extremely robust to focal plane array noise and scintillation even in the case of 10s of signal photons per pixel with a camera gain of 183 ph/adu and a read noise of 300 e- rms. In addition, when using the interferometric wave-front sensor with a pixilated MEMS deformable mirror it is not necessary to perform a reconstruction of the wave-front allowing the speeds to be significantly higher than with a conventional adaptive optics system. This latter trait will be critical for the next generation of fusion laser systems operating at repetition rates greater than 10 hz and with target injection speeds higher than 200 m/sec which will necessitate adaptive optics systems to perform tracking at greater than 20 khz.

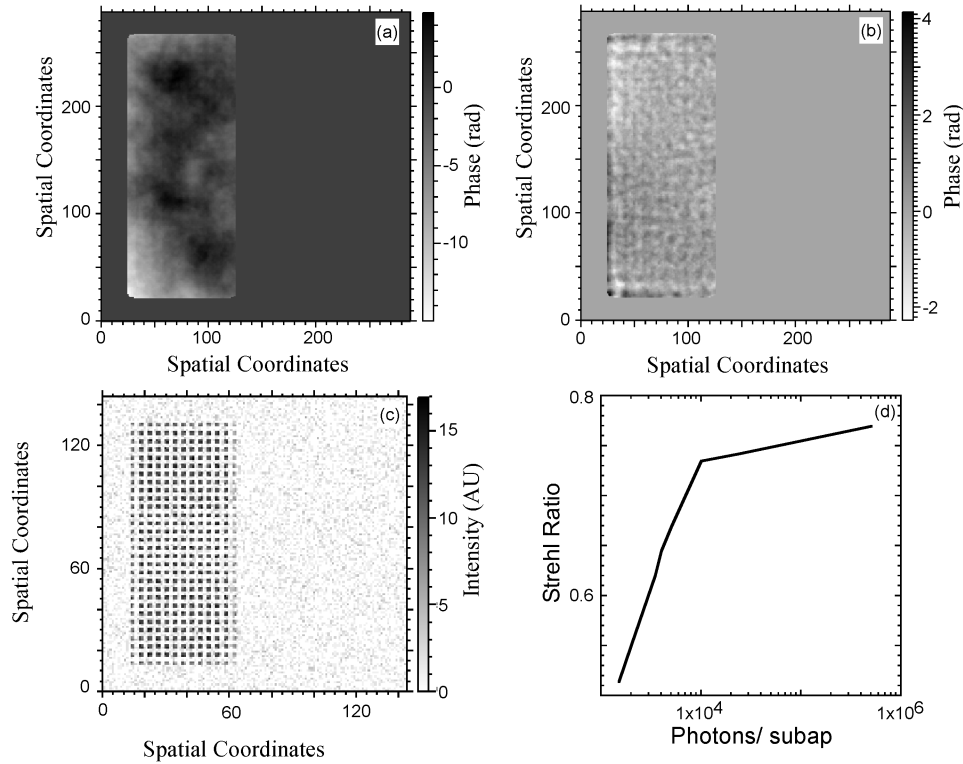


Fig. 19 Closed-loop Shack-Hartmann adaptive optics system with continuous phase sheet MEMS device. The original phase profile on the laser is shown in Fig. 19a. The residual phase after 30 iterations at a gain of 0.3 is shown in Fig. 19b. The Hartmann spots are displayed in Fig. 19 c for a photon/subap value of 12k. The simulations were performed with a camera gain of 183 ph/adu and a read noise of 300 e- rms. The Strehl ratio as a function of photons/subap is given in Fig. 19 d illustrating that the Shack-Hartmann wave-front sensor requires considerably more signal photons than the interferometric wave-front sensor.

4. SUMMARY

This article presented the design and expected performance of an interferometric adaptive optics testbed that will be implemented on the NIF quad comprising both the advanced radiography capability and the fast ignition drive optics. The fast ignition operation places requirements on the energy encircled within a 40 μm diameter that can not be met without pistoning beam pairs which is readily accomplished with the interferometric wave-front sensor. The operation of the interferometric AO system on the NIF laser was presented under two different scenarios. These scenarios include operating the AO system at a rate governed by the existing, or slightly modified, plasma-electrode pockel cell (PEPC) electronics up to a hertz and a scenario whereby the interferometric system is operated at speeds in excess of 5 khz with significant changes made to the PEPC drive electronics. The operating regime for the interferometric adaptive optics system in terms of tip/tilt correction and wave-front gradients was investigated and the penalties for various conditions such as detector or window induced fringing and incorrect background subtraction were determined. Simulations of the

interferometric adaptive optic system indicate that the interferometric WFS achieves encircled energy ratios of ~ 0.5 , implying ~ 4 kJ of energy for ~ 8 kJ in the eight beams. This does not, however, include additional energy from grazing incidence reflection and refraction of the remaining energy towards the end of the cone, contribution from electrons generated higher up in the cone or improvement to the MEMS device itself reducing the residual MEMS phase profile. The performance of the interferometric adaptive optics system was compared with a conventional Shack-Hartmann wave-front sensor and found that the interferometric AO system provided comparable performance with nearly three orders of magnitude fewer signal photons given the noise parameters for the detector. This reduced energy level is extremely important for cryogenic targets and enables the use of fiber optic backlighters in addition to scattering spheres. In addition the interferometric wave-front sensor is capable of tip/tilt, piston and high order wave-front correction with a single wave-front sensor and deformable mirror without requiring global wave-front reconstruction enabling it to reach speeds in excess of 10 kHz.

ACKNOWLEDGEMENTS

The authors would like to thank Everett Utterback and Steve Jones for assistance in programming the data acquisition system for the testbed. This work was performed under the auspices of the U.S. Department of Energy by Lawrence Livermore National Laboratory under Contract DE-AC52-07NA27344.

REFERENCES

- [1] R. A. Zacharias, N. R. Beer, E.S. Bliss, S. C. Burkhart, S. J. Cohen, S. B. Sutton, R. L. Van Atta, S. E. Winters, J. T. Salmon, M. R. Latta, C. J. Stolz, D. C. Pigg, and T. J. Arnold, "Alignment and wavefront control systems of the National Ignition Facility," *Opt. Eng.* **43** (12), 2873 (2004).
- [2] D.M. Pennington, C.G. Brown, T.E. Cowan, S.P. Hatchett, E. Henry, S. Herman, M. Kartz, M. Key, J. Koch, A.J. Mackinnon, M.D. Perry, T.W. Phillips, M. Roth, T.C. Sangster, M. Singh, R.A. Snavely, M. Stoyer, B.C. Stuart, and S.C. Wilks, "Petawatt Laser System and Experiments," LLNL Report No. UCRL-JC-140019, 2000.
- [3] Robert Hartley, Michael Kartz, William Behrenclt, Andy Hines, George Pollock, Erlan Bliss, Thad Salmon, Scott Winters, Bruno Van Wonterghem, and Richard Zacharias, "Wavefront correction for static and dynamic aberrations to within 1 second of the system shot in the NIF Beamlet demonstration facility," *SPIE* **3047**, 294 (1997).
- [4] Ji-Ping Zou, Anne-Marie Sautivet, Jérôme Fils, Luc Martin, Kahina Abdeli, Christian Sauteret, and Benoit Wattellier, "Optimization of the dynamic wavefront control of a pulsed kilojoule/nanosecond-petawatt laser facility," *Applied Optics* **47** (5), 704 (2008).
- [5] C.N. Danson, P.A. Brummitt, R.J. Clarke, J.L. Collier, B. Fell, A.J. Frackiewicz, S. Hancock, S. Hawkes, C. Hernandez-Gomez, P. Holligan, M.H.R. Hutchinson, A. Kidd, W.J. Lester, I.O. Musgrave, D. Neely, D.R. Neville, P.A. Norreys, D.A. Pepler, C.J. Reason, W. Shaikh, T.B. Winstone, R.W.W. Wyatt, and B.E. Wyborn, "Vulcan Petawatt—an ultra-high-intensity interaction facility," *Nucl. Fusion* **44**, 239 (2004).
- [6] K.L. Baker, E.A. Stappaerts, D. Gavel, S.C. Wilks, J. Tucker, D.A. Silva, J. Olsen, S.S. Olivier, P.E. Young, M.W. Kartz, L.M. Flath, P. Kruelevitch, J. Crawford, and O. Azucena, "Breadboard Testing of a Phase Conjugate Engine with an Interferometric Wave-Front Sensor and a MEMS-Based Spatial Light Modulator," *Appl. Opt.* **43** (30), 5585 (2004).
- [7] K.L. Baker, E.A. Stappaerts, D. Gavel, S.C. Wilks, J. Tucker, D.A. Silva, J. Olsen, S.S. Olivier, P.E. Young, M.W. Kartz, L.M. Flath, P. Kruelevitch, J. Crawford, and O. Azucena, "High-speed horizontal-path atmospheric turbulence correction using a large actuator-number MEMS spatial light modulator in an interferometric phase conjugation engine," *Opt. Lett.* **29** (15), 1731 (2004).
- [8] K.L. Baker, E.A. Stappaerts, S.C. Wilks, P.E. Young, D. Gavel, J. Tucker, D.A. Silva, and S.S. Olivier, "Open and Closed-Loop Aberration Correction using a Quadrature Interferometric Wave-Front Sensor," *Opt. Lett.* **29** (1), 47 (2004).
- [9] James Millerd, John Hayes, Michael North-Morris, Matt Novak, and James Wyant, "Pixelated Phase-Mask Dynamic Interferometer," *SPIE* **5331**, 304 (2004).
- [10] K.L. Baker, E.A. Stappaerts, S.C. Wilks, D. Gavel, P.E. Young, J. Tucker, D.A. Silva, S.S. Olivier, and J. Olsen, "Performance of a phase-conjugate-engine implementing a finite-bit phase correction," *Opt. Lett.* **29** (5) (2004).
- [11] P.A. Arnold, C.W. Ollis, A. Hinz, C. Robb, K.A. Primdahl, J.J. Watson, M.D. O'Brien, W.G. Funkhouser, P.J. Biloft, R.T. Shelton, W.C. Tapley, and W.J. DeHope, "Deployment, commissioning and operation of plasma electrode Pockels cells in the National Ignition Facility," *SPIE* **5341**, 156 (2004).

- [12] Malgorzata Kujawinska, [*Interferogram Analysis*], edited by David W Robinson and Graeme T Reid (Institute of Physics Publishing, Bristol and Philadelphia, 1993).
- [13] K.L. Baker and D.A. Silva, "Evaluation of Two-Dimensional Phase Unwrapping Algorithms for Interferometric Characterization of Liquid-Crystal Spatial Light Modulators," *The Open Optics Journal* **2**, 48 (2008).
- [14] R.M. Goldstein, H.A. Zebker, and C.L. Werner, Satellite radar interferometry: two-dimensional phase unwrapping *Radio Science* **23** (4), 713 (1988).
- [15] Dennis C. Ghiglia and Mark D. Pritt, [*Two-Dimensional Phase Unwrapping*]. (John Wiley & Sons, Inc., New York, 1998).
- [16] G. Chanan, M. Troy, F. Dekens, S. Michaels, J. Mast, and D. Kirkman, "Phasing the mirror segments of the Keck telescopes: the broadband phasing algorithm," *Appl. Opt.* **37**, 140 (1998).